

SEISMIC HALOS AROUND ACTIVE REGIONS: A MAGNETOHYDRODYNAMIC THEORY

SHRAVAN M. HANASOGE

W. W. Hansen Experimental Physics Laboratory, Stanford University, Stanford, CA 94305; shravan@stanford.edu
Received 2007 December 20; accepted 2008 February 28

ABSTRACT

Comprehending the manner in which magnetic fields affect propagating waves is a first step toward constructing accurate helioseismic models of active region subsurface structure and dynamics. Here we present a numerical method for computing the linear interaction of waves with magnetic fields embedded in a solar-like stratified background. The ideal magnetohydrodynamic (MHD) equations are solved in a three-dimensional box that straddles the solar surface, extending from 35 Mm below the photosphere to 1.2 Mm into the atmosphere. One of the challenges in performing these simulations involves generating a magnetohydrostatic (MHS) state wherein the stratification assumes horizontal inhomogeneity in addition to the strong vertical stratification associated with the near-surface layers. Keeping in mind that the aim of this effort is to understand and characterize linear MHD interactions, we discuss a means of computing statically consistent background states. Power maps computed from simulations of waves interacting with thick flux tubes that have peak photospheric field strengths of 600 and 3000 G are presented. Strong modal power reduction in the “umbral” regions of the flux tube enveloped by a halo of increased wave power is seen in the simulations with the thick flux tubes. These enhancements are also seen in Doppler velocity power maps of active regions observed in the Sun, which leads us to propose that the halo has MHD underpinnings.

Subject headings: hydrodynamics — Sun: helioseismology — Sun: interior — Sun: oscillations — waves

1. INTRODUCTION

The complexity of the solar background state, subtleties in the dynamics of wave propagation in the near-surface layers, and the inherently anisotropic, tensorial nature of magnetic fields disadvantage analytically driven MHD studies. Theoretical models of MHD interactions in flux concentrations have proven to be somewhat restrictive in terms of the scope of problems addressed, given the effort required to construct these models. In this regard, numerical forward modeling of wave propagation (e.g., Hanasoge et al. 2006, 2007b; Cameron et al. 2007; Shelyag et al. 2007; Khomenko et al. 2008; Parchevsky & Kosovichev 2007a) has been relatively successful at making sense of the sometimes highly counterintuitive wave phenomena observed in the Sun.

Accurately deconstructing the subsurface structure and dynamics of active regions is a difficult task. Since the development of methods of time-distance helioseismology (Duvall et al. 1993; Gizon & Birch 2005) and the subsequent investigations into the nature of the sunspot underbelly (Duvall et al. 1996; Kosovichev & Duvall 1997; Couvidat et al. 2006), there have been several arguments attempting to establish either the significance of MHD interactions in sunspot structure and dynamics inversions (e.g., Lindsey & Braun 2005; Schunker et al. 2005) or the contrary (Zhao & Kosovichev 2006). Recent theories (Braun & Birch 2006) argue that most of the observed wave phase shifts in sunspot regions occur in a thin subphotospheric region of 1 Mm depth, where magnetic field effects are putatively the largest. The implication is that the causative mechanisms behind observed wave phase shifts may have been misidentified, a conclusion echoed by Hanasoge et al. (2007a), who demonstrate that wave source suppression due to convective blocking in sunspots can also contribute to the creation of time shifts (see also Gizon & Birch 2002). Moreover, wave phase shifts inferred in regions of strong magnetic fields from Michelson Doppler Imager (MDI; Scherrer et al. 1995) observations (e.g., Duvall et al. 1996) are difficult to interpret because of substantial changes in the line formation height due to profound alterations in the thermal structure of the under-

lying plasma. On the positive side, the prevalence of computing resources and numerical methodologies now afford us the ability to conduct investigations that may not have been possible a decade ago. Developing an interaction theory of waves and magnetic fields will allow us to perform more consistent studies of sunspot structure and dynamics.

The reduction in acoustic oscillation power in sunspot regions (e.g., Lites et al. 1982) has been the subject of extensive observations, with several theories put forth to explain this phenomenon (e.g., Hindman et al. 1997; Parchevsky & Kosovichev 2007b). Hindman et al. (1997) have discussed several plausible mechanisms that may be contributing to the power reduction, but the participatory extents are as yet unknown. On a related issue, a number of studies have focused on placing observational constraints on the degree of wave absorption in sunspots (e.g., Braun et al. 1987; Bogdan et al. 1993; Braun 1995; Cally 1995). The technique discussed here provides an independent manner of investigating all of these issues. Acoustic or seismic enhancements (or halos, as they are termed in this paper) are ubiquitously seen in both velocity and intensity observations, encircling active regions (e.g., Braun et al. 1992; Brown et al. 1992; Balthasar et al. 1998; Hindman & Brown 1998; Donea et al. 2000; Nagashima et al. 2007). Some authors (Brown et al. 1992; Donea et al. 2000) have speculated that they originate from enhanced source activity in the vicinity of the active region. In this paper, we present power maps from simulations of waves interacting with moderate to strong magnetic fields; acoustic halos are clearly seen in these images, implicating an MHD-based mechanism.

On a very different scale but of equal importance are small magnetic elements and thin flux tubes. The dynamical emergence and disappearance of these flux tubes provides us with insights into the photospheric dynamo (e.g., Cattaneo 1999). In a bid to understand the structure of these flux tubes, Duvall et al. (2006) analyzed MDI observations of thousands of independent small magnetic elements, thereby developing a highly resolved statistical picture of the associated wave scattering. Understanding the nature of the interaction between thin flux tubes and waves may

allow us to recover details of the flux tube structure from the scattering information. Forward models of wave interactions with thin flux tubes (e.g., Bogdan & Cally 1995; Bogdan et al. 1996; Gizon et al. 2006; Hanasoge et al. 2008) can then be constructed in order to place constraints on the subsurface magnetic field distribution. Models of this sort can be used in theoretical studies of flux emergence (e.g., Cheung et al. 2006).

In this regard, a first step is to devise a sufficiently general manner of computing wave propagation in a magnetized plasma. The linearized ideal MHD equations provide a reasonable starting point, since MHD oscillations in the photosphere and below are governed by predominantly linear physics (e.g., Bogdan 2000). Cally & Bogdan (1997), Rosenthal & Julien (2000), and Cally (2000) performed MHD simulations in two dimensions in order to study rates of mode absorption in magnetic flux tubes. Subsequently, Cameron et al. (2007) developed and validated numerical techniques with which to perform three-dimensional linear MHD computations, with a focus on recovering the magnetic field distribution on the basis of wave-scattering measurements. The assumptions of linear wave propagation and time stationarity of the background state are common threads between this work and that of the above-cited authors.

High-order numerical accuracy is a minimum requirement for computational work. The linear calculation discussed here does not face the same restrictions as would a nonlinear counterpart, where the presence of shocks makes it quite difficult to raise the order of the numerical scheme without introducing instabilities. We discuss the methods employed to spatiotemporally evolve solutions of the ideal MHD equations in § 2. Subsequently, an empirical method to generate stable MHS states is introduced in § 3, with an illustration of one such state: a flux tube with a peak photospheric field strength of 600 G. Results of wave simulations with some flux tubes—specifically, the phenomena of wave power reduction and enhancement—are discussed in § 3.1. Finally, we summarize and conclude in § 4.

2. COMPUTATIONAL METHOD

Similar to the forward models of the solar wave field developed in Hanasoge et al. (2006), Hanasoge et al. (2007b), and Hanasoge (2007), we start by linearizing and modifying the ideal MHD equations in the following manner:

$$\partial_t \rho = -\nabla \cdot (\rho_0 \mathbf{v}) - \Gamma \rho, \quad (1)$$

$$\begin{aligned} \partial_t \mathbf{v} = & -\frac{1}{\rho_0} \nabla p - \frac{\rho}{\rho_0} g \hat{\mathbf{e}}_z \\ & + \frac{\zeta(z)}{4\pi\rho_0} [(\nabla \times \mathbf{B}_0) \times \mathbf{B} + (\nabla \times \mathbf{B}) \times \mathbf{B}_0] + \mathbf{S} - \Gamma \mathbf{v}, \end{aligned} \quad (2)$$

$$\partial_t p = -\mathbf{v} \cdot \nabla p_0 - \rho_0 c^2 \nabla \cdot \mathbf{v} - \Gamma p, \quad (3)$$

$$\partial_t \mathbf{B} = \zeta \nabla \times (\mathbf{v} \times \mathbf{B}_0) - \Gamma \mathbf{B}, \quad (4)$$

$$\nabla \cdot \mathbf{B} = 0, \quad (5)$$

where ρ denotes density (unless stated otherwise, the subscript “0” indicates a time-stationary background quantity, whereas unsubscripted terms fluctuate), p is the pressure, $\mathbf{B} = (B_x, B_y, B_z)$ is the magnetic field, $\mathbf{v} = (v_x, v_y, v_z)$ is the vector velocity, $g = g(z)$ is gravity with direction vector $-\hat{\mathbf{e}}_z$, $c = c(x, y, z)$ is the sound speed, $\Gamma = \Gamma(x, y, z) > 0$ is a damping sponge that enhances wave absorption at all horizontal and vertical boundaries (see Fig. 1), $\zeta(z)$ is a Lorentz force “controller” (R. Cameron 2007 and R. Stein 2007, private communications), and \mathbf{S} is the source term. The controller term ζ (see Fig. 2a) is such that it is con-

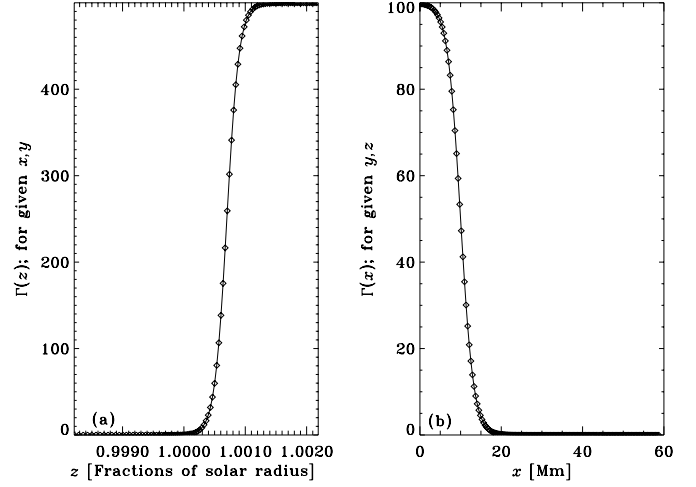


FIG. 1.—Plot of the function $\Gamma(x, y, z)$ from eqs. (1)–(4). In panel *a*, the value of Γ at a location far away from the side boundaries is plotted as a function of z . The vertical boundaries of the computational box are at $z = 0.95$ and $1.002 R_\odot$; although it is not shown here, the behavior of Γ at the lower boundary is qualitatively similar to that in panel *a*. In panel *b*, we show the variation of Γ with the horizontal coordinate x at a location far away from the vertical and y boundaries, with $x = 0$ serving as one of the side boundaries. As waves approach within 20 Mm of the horizontal and/or 1 Mm of the vertical boundaries, they start to experience strong damping from the $-\Gamma$ term.

stant (=1) over most of the interior but decays rapidly with height above the photosphere. Note that ζ is also present in equation (4): as the influence of the magnetic field on the fluid decreases (eq. [2]), so must the effect of the fluid on the magnetic field. For further discussion on the reasoning behind this term, see § 2.1.

We employ a Cartesian coordinate system (x, y, z) , where $\hat{\mathbf{e}}_z$ denotes the unit vector along the vertical or z -axis and t is time. Because of the presence of a spatially varying magnetic structure, the background pressure, density, and sound speed adopt a fully three-dimensional spatial dependence. In sequential order, equations (1)–(3) enforce mass, momentum, and energy conservation, respectively, while equation (4) is the induction equation. Equation (5) assures us that magnetic monopoles do not exist. In interior regions of the computational box (away from the boundaries), solutions to the above equations are adiabatic, since the damping terms decay to zero here. The source term \mathbf{S} is a spatiotemporally varying function, the structure of which has been discussed in some detail in Hanasoge & Duvall (2007) and Hanasoge et al. (2007b). Essentially, it is a phenomenological model for the multiple-source wave excitation picture that is observed (inferred, perhaps) in the Sun. The background vertical stratification is an empirically derived (Hanasoge et al. 2006), convectively stabilized form of model S (Christensen-Dalsgaard et al. 1996).

The base hydrodynamic method remains unchanged from that of Hanasoge et al. (2007b): spatial derivatives are calculated using sixth-order compact finite differences (Lele 1992), and time evolution is achieved through the repeated application of an optimized second-order five-stage Runge-Kutta scheme (Berland et al. 2006). The temporal order of accuracy is dropped, because the time step (2 s) is much smaller than the period of the waves studied here. The boundaries are lined with damping sponges in order to absorb (i.e., damp) outgoing waves (Fig. 1). This is to prevent any scattered waves from reentering the computational domain, as would be the case with periodic boundaries. Our attempt to extend the base scheme to compute the magnetic field terms in equations (2) and (4) was successful. All derivatives, including the magnetic field terms, are estimated using sixth-order compact finite differences, thus maintaining a high order of spatial accuracy. It was observed

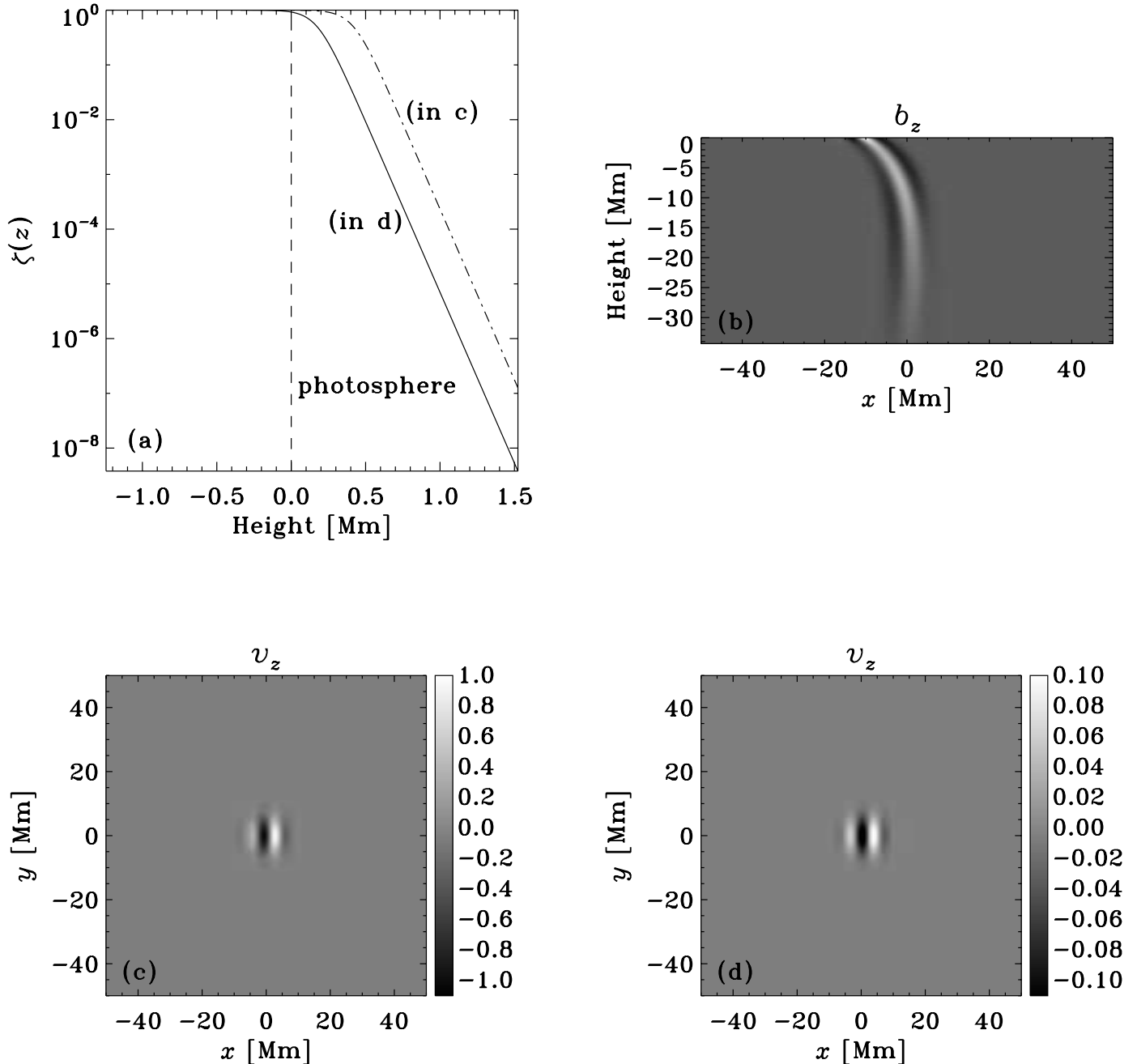


FIG. 2.—Dependence of wave scattering on $\zeta(z)$ (eqs. [2] and [4]). Panel *a* shows functional forms of ζ , used in two different MHD wave test simulations, termed *c* and *d*. The initial condition, which is the same for both simulations, is a plane wave packet localized at $x = -30$ Mm, $z = -0.2$ Mm. Panel *b* shows fluctuations in b_z , which arise due to the interaction of the wave with the flux tube. Panels *c* and *d* display the instantaneous normalized vertical velocity [$v_z(x, y, z = 0.2$ Mm, $t = 31$ minutes), units are arbitrary] of the scattered waves extracted at a height of 200 km above the photosphere from simulations *c* and *d*, respectively. An order-of-magnitude difference can be seen between the two cases, indicating that the results are somewhat sensitively dependent on the chosen form of ζ .

that the $\nabla \cdot \mathbf{B}$ term was of a low magnitude, $\lesssim 10^{-7}$ pixel $^{-1}$ (despite the presence of the ζ term in the induction equation), and therefore harmless (e.g., Tóth 2000; Abbett 2007). Moreover, the presence of the damping term $\Gamma \mathbf{B}$ ensures that $\nabla \cdot \mathbf{B}$ is forced to decay in the damping sponge layers. Validation in one and two dimensions of the essential numerical method (i.e., without the ζ or Γ terms) is discussed in the Appendix.

2.1. Lorentz Force Controller

As stated in § 2, ζ retains a value of 1 in the interior and decreases with height above the photosphere (Fig. 2*a*). It attempts to achieve a two-fold purpose: (1) to reduce the Lorentz force with increasing altitude above the photosphere and (2) to prevent

the onset of negative pressure effects. The mean hydrodynamic pressure and density in the Sun drop exponentially with height in the atmosphere that immediately overlays the photosphere. In our calculations of MHS states (§ 3), it was nearly impossible to prevent complete pressure and density evacuation in the interiors of flux tubes of large-magnitude field strengths (1500 G and more; sadly, nowhere close to the umbral field strengths of up to 6100 G that have been observed in sunspots by Livingston et al. 2006). Moreover, the equilibrium horizontal pressure distribution takes on strange forms, with the pressure at the center of a flux tube attaining larger values than the ambient value when the flux tube radius is forced to increase faster than the corresponding potential field configuration. In the Sun, the presence of magnetic

field everywhere and the phenomenon of flux tubes merging in the atmosphere (e.g., Pneuman et al. 1986; Bogdan et al. 1996) help to reduce large gradients in the magnetic field, thereby preventing complete evacuation in active regions and sunspots while not requiring the flux tubes to flare out too rapidly. We attempt to simulate this (criterion 1) through the $\zeta(z)$ term. However, since the equilibrium structure of an active region is as yet unknown, it is not possible to determine how realistic a chosen functional form of ζ is.

To determine the impact of $\zeta(z)$ on the wave field, we simulate the interaction of a wave packet with a relatively weak flux tube (~ 100 G at the photospheric level) in a solar-like stratified medium. Three simulations are performed, a quiet simulation (“q”) without any magnetic field and two (“c” and “d”) with different functional forms of ζ , one form of ζ decaying more rapidly with height than the other (shown in Fig. 2a). The initial condition for all simulations was chosen to be a Gabor wavelet-shaped disturbance in v_z localized at $(x, z) = (-30, -0.2)$ Mm, at all values of y . At approximately the instant when the wave packet reaches the center of the flux tube [located at $(x, y) = (0, 0)$ Mm], we display snapshots of $v_z^c - v_z^q$ and $v_z^d - v_z^q$ in Figures 2c and 2d, respectively, where the superscripts refer to the simulation index (q, c, or d). In the presence of a linear scatterer, one may view the velocity field as being associated with both an incident and a scattered wave; in this situation, v_z^q is the incident wave velocity, and the scattered wave velocities are described by the differences $v_z^{c,d} - v_z^q$. It is clear from Figures 2c and 2d that the extent of the scatter in the simulation where ζ decays higher up in the atmosphere (simulation c) is greater by an order of magnitude than that in simulation d. Perhaps mode conversion, which has been theoretically shown to become significant when the plasma β starts to drop, is at play (e.g., Bogdan et al. 1996; Cally & Bogdan 1997; Crouch & Cally 2003). It may also be that the magnetic field changes the v_z eigenfunction more significantly in one case than the other. Essentially, this experiment tells us that capturing wave interactions in an active region is somewhat sensitively dependent on the choice of the ζ function, or, in other words, on the atmospheric magnetic field distribution in the vicinity. It underlines the necessity of viewing this effort as more qualitative than quantitative, since conclusions of the latter sort require one to explore a formidable parameter space.

3. MHS STATES

Generating MHS states in stratified media can be a nontrivial task (e.g., Pneuman et al. 1986; Pizzo 1990; Beliën et al. 2002; Khomenko et al. 2008). Fully consistent approaches that involve relaxing the MHD equations to low-energy equilibria are difficult to implement. Moreover, such calculations are beyond the scope of this effort; we are interested less in the MHS states themselves than in the manner in which waves interact with them. We invoke the Schlüter & Temesváry (1958) self-similar magnetic field geometry and ignore both radiative transfer effects and the satisfaction of the equation of state. We also remind the reader that the background stratification has been altered to prevent the onset of uncontrolled linear growth of convective instabilities, thus changing the opacities in a nonphysical manner. The Schlüter & Temesváry (1958) approximation tells us that making the following choices for the radial and vertical magnetic fields, B_r and B_z , assures us of the satisfaction of equation (5) (e.g., Schüssler & Rempel 2005):

$$B_z = M\psi(z)e^{-r^2\psi(z)}, \quad (6)$$

$$B_r = -M\frac{r}{2}\psi' e^{-r^2\psi(z)}, \quad (7)$$

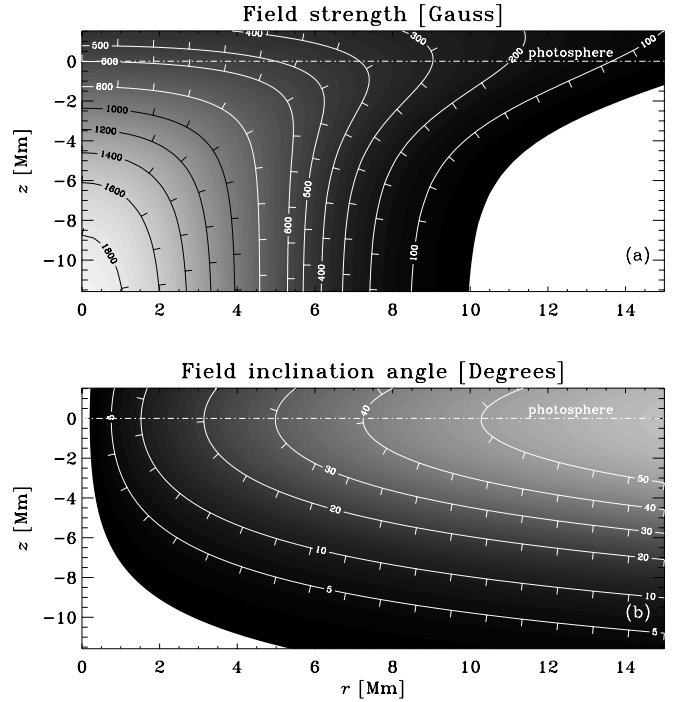


FIG. 3.—Example of a flux tube generated according to the recipe of § 3. Panel *a* shows the field strength, $|B| = (B_r^2 + B_z^2)^{1/2}$; panel *b* shows the field inclination angle, $\arctan(B_r/B_z)$. Perpendicular to the contour lines are spokes that point in the direction of the downhill gradient. The pressure and density remain positive over the entire domain. Field strength magnitudes, in units of gauss, and inclination angles, in units of degrees, are indicated along the contour lines.

where $\psi' = d\psi/dz$. The above equations (eqs. [6] and [7]) are in cylindrical geometry; the quantities r and z refer to the horizontal radial and vertical coordinates, where $r = 0$ coincides with the center of the flux tube; M is a term that controls the magnitude of the magnetic field and hence the flux ($=\pi M$); and $\psi(z)$ determines the horizontal extent of the flux tube and the rate at which the flux tube spreads with altitude. The zeroth-order MHS equations in cylindrical coordinates, which are obtained by dropping the time and azimuthal dependencies in equation (2), reduce to

$$0 = -\partial_r p + \zeta \frac{B_z}{4\pi} (\partial_z B_r - \partial_r B_z) \quad (8)$$

along the horizontal (r) direction, and in the vertical (z) direction,

$$0 = -\partial_z p - \zeta \frac{B_r}{4\pi} (\partial_z B_r - \partial_r B_z) - \rho g. \quad (9)$$

Equation (8) is integrated over r from 0 to infinity to obtain the following equation:

$$p_c(z) = p_\infty(z) + \frac{M^2 \zeta}{4\pi} \left(\frac{1}{16} \frac{\psi'^2}{\psi} - \frac{1}{8} \psi'' + \frac{\psi^2}{2} \right), \quad (10)$$

where $p_c(z)$ is the pressure along the axis (center line) of the flux tube and $p_\infty(z)$ is the hydrostatic pressure far away from the magnetic region. The horizontal pressure distribution at a given value of z can now be computed by integrating equation (8) from the center outward:

$$p(r', z) = p_c(z) + \frac{\zeta}{4\pi} \int_0^{r'} dr B_z (\partial_z B_r - \partial_r B_z); \quad (11)$$

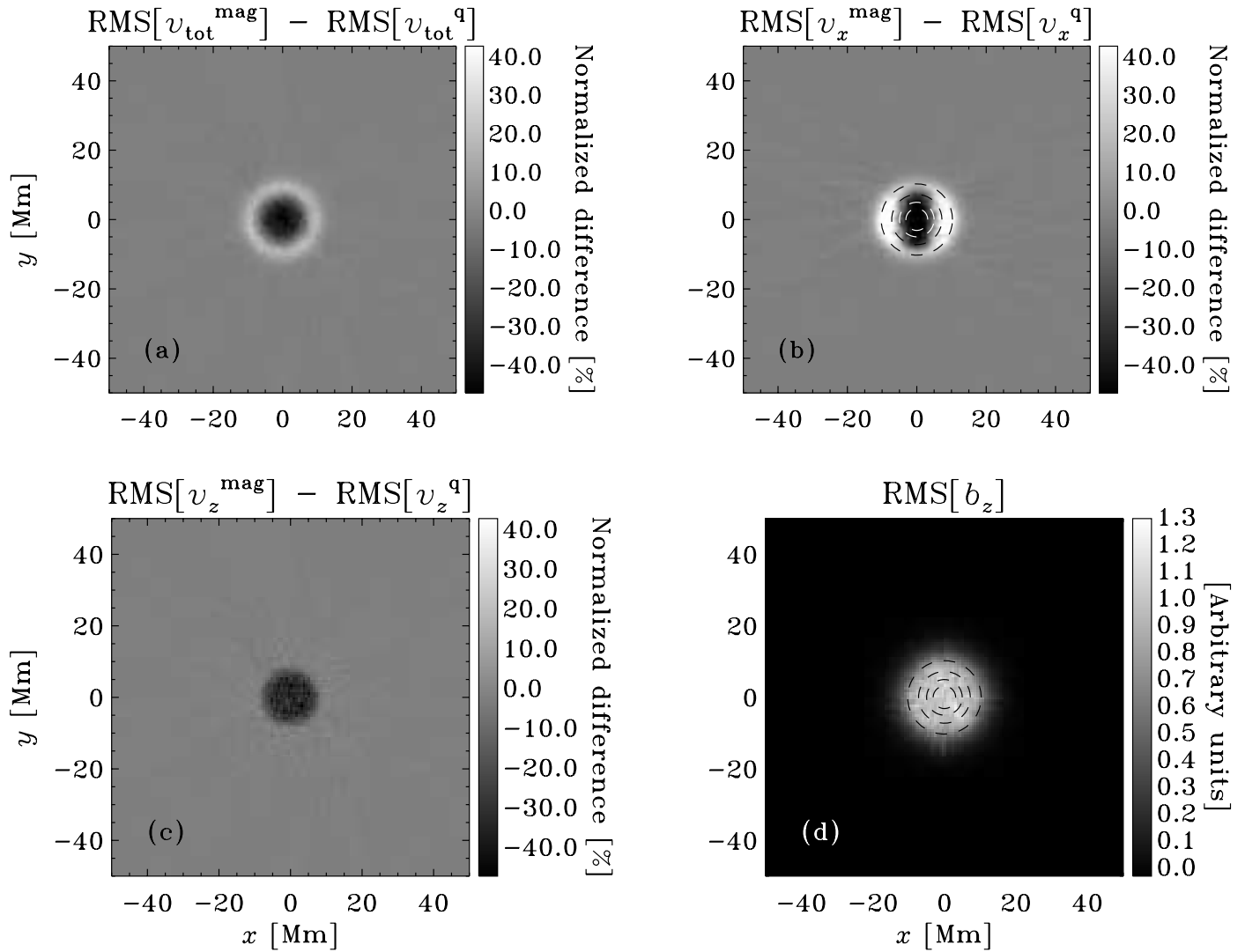


FIG. 4.—Changes in acoustic power due to MHD interactions (600 G case). Two simulations were performed: one quiet (“q”), without perturbation, and one using an MHD calculation (“mag”), with the flux tube of Fig. 3 embedded in the computational domain. Panel *a* shows the rms differences of the total velocity, $v_{\text{tot}} = (v_x^2 + v_y^2 + v_z^2)^{1/2}$, between the quiet and magnetic simulations. Panels *b* and *c* display the rms differences seen in v_x and v_z , while panel *d* shows the rms values of the vertical magnetic field fluctuations, b_z . Each power difference is normalized by the mean value of the rms power of the corresponding quantity (i.e., v_x , v_z , or v_{tot}) derived from the quiet simulation. With increasing radius, the contours in panels *b* and *d* show the locations at which the field inclination is [20°, 30°, 40°, 50°]. The field strengths at these contours are [560, 495, 397, 240] G, respectively. Outside a region of substantial decrease in wave oscillation amplitudes, a halo corresponding to an increase in the rms power can be seen.

thus, the entire pressure field can be recovered through this procedure. Simplifying equation (9), we can obtain the density field from the pressure distribution:

$$\rho(r, z) = -\frac{1}{g} \left[\partial_z p + \zeta \frac{B_r}{4\pi} (\partial_z B_r - \partial_r B_z) \right]. \quad (12)$$

Therefore, upon specifying the parameters M and $\psi(z)$ in equations (6) and (7), one can obtain a self-consistent MHS solution that satisfies the criteria of $\nabla \cdot \mathbf{B} = 0$ and magnetohydrostatic balance. One must be careful, however, to ensure positive pressure and density in equations (11) and (12) at all points in the computational domain. In Figure 3, we show an example of a flux tube that attains a peak strength of 600 G at the photospheric level; the inclination of the field at distances away from the center is also shown.

3.1. Seismic Power Deficits and Halos

Theoretical expectations dictate a decrease in modal power in magnetic regions due to mode absorption and MHD-wave

coupling. Using identical realizations of the source function \mathcal{S} (eq. [2]), we perform two simulations: a “quiet” run with no perturbation and an MHD counterpart (the “mag” run) that has the flux tube described in Figure 3 embedded at the center of a computational box of size 100 Mm \times 100 Mm \times 35 Mm. In Figure 4 we show the difference in the time-averaged rms wave power between the quiet simulation and its magnetic counterpart, normalized by the mean value of the rms wave power of the quiet case. Both runs were 12 hr long. Because the realizations are identical, the MHD interactions are the dominant component of the quantity $\text{RMS}^{\text{mag}} - \text{RMS}^{\text{q}}$. It is interesting to note that, depending on the variable under study, the simulations predict strong variations in the nature and degree of the change in the wave power. For example, the rms differences in the total velocity, $v_{\text{tot}} = (v_x^2 + v_y^2 + v_z^2)^{1/2}$, show the presence of a large reduction in wave power surrounded by an intense halo, whereas the rms decrease as seen in v_z is systematically weaker and has an almost invisible halo. Figures 4*b* and 4*d* show contours of increasing radii that correspond to field inclinations of [20°, 30°, 40°, 50°].

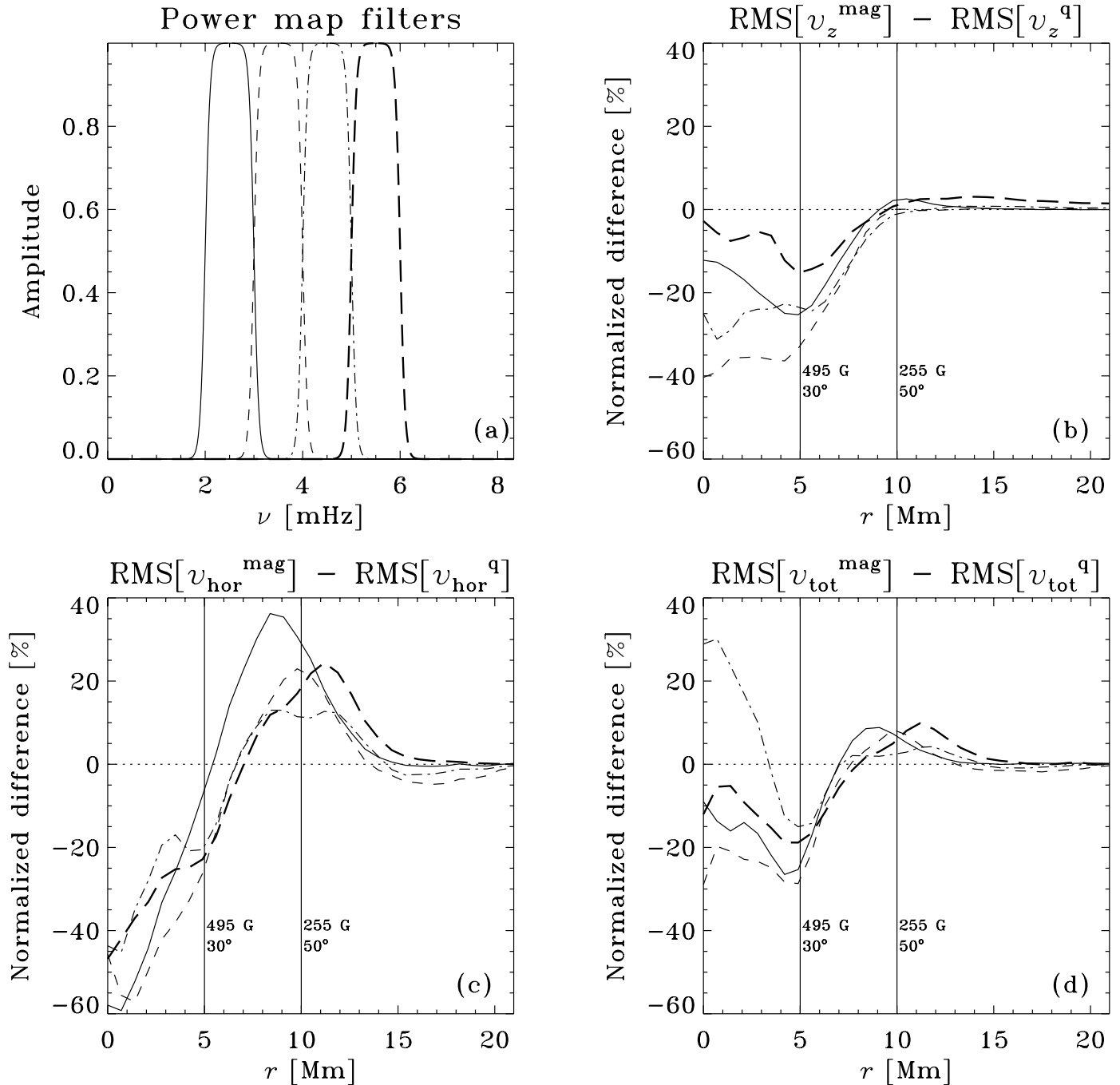


FIG. 5.—Azimuthal averages of the frequency-filtered wave power maps (600 G case). Panel *a* shows four filters with bandpasses of 2–3, 3–4, 4–5, and 5–6 mHz. Panels *b*, *c*, and *d* display the azimuthally averaged (around the center of the flux tube) normalized noise-subtracted power maps of the quantities v_z , $v_{\text{hor}} = (v_x^2 + v_y^2)^{1/2}$, and v_{tot} , respectively. Each power difference is normalized by the mean value of the rms power of the correspondingly filtered quiet simulation. The quantity v_z exhibits the least change in the rms power of all the variables shown here. Note that v_{hor} and v_{tot} are more difficult to interpret because sign information is lost ($v_{\text{hor}}^{\text{q,mag}}, v_{\text{tot}}^{\text{q,mag}} \geq 0$). The two vertical lines in panels *b*, *c*, and *d* are labeled with the magnetic field strength and the inclination at these locations.

The halo is seen at inclinations of 50° and higher, while a strong reduction in wave power is observed at smaller angles. Also, the robustness of the halo was ensured by verifying its reappearance in a simulation that used an alternate numerical method, namely, a second-order constrained transport (CT) technique (Evans & Hawley 1988).

In order to study these effects further, we computed power maps in four different frequency bandpasses: 2–3, 3–4, 4–5, and 5–6 mHz. Three different components of the velocity were used in the calculations: v_z , v_{tot} , and $v_{\text{hor}} = (v_x^2 + v_y^2)^{1/2}$. We subtract the power maps of the quiet simulation computed in the

same bandpasses in order to reduce the realization noise. The frequency filters used to recover the power maps and the azimuthally averaged power profiles (about the flux tube center) obtained subsequently are shown in Figure 5. Noteworthy aspects are that v_{hor} contains the most intense halos, v_{tot} shows a dramatic increase in rms power in the range 4–5 mHz around the “umbral” region of the flux tube (defined as that within a distance of 8 Mm from the center of the flux tube), and the rms variation in v_z is somewhat limited in comparison to the rest. These effects (or some fraction thereof) could be attributed to changes in the eigenfunctions caused by the magnetic fields. The appropriate

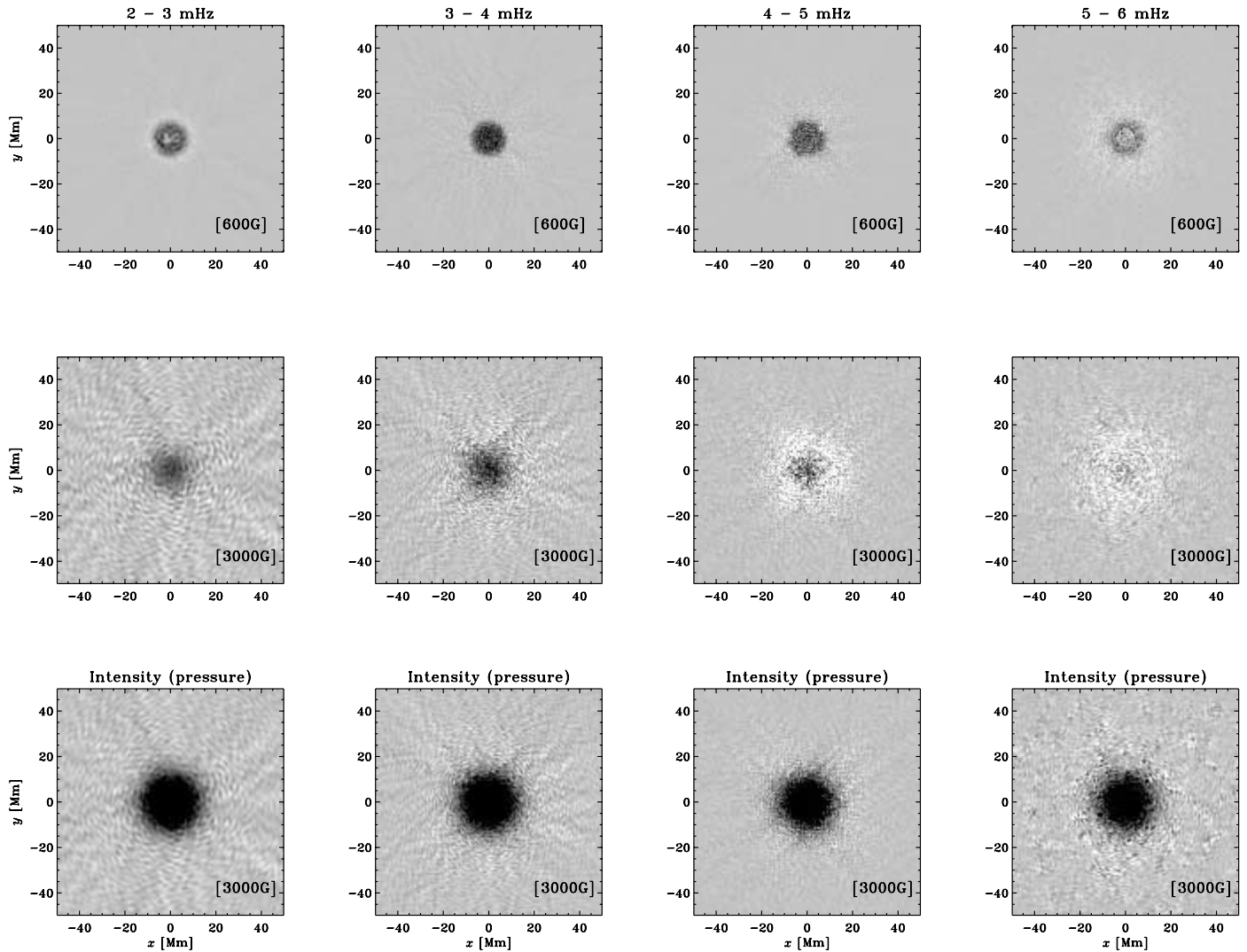


FIG. 6.—Changes in acoustic power due to MHD interactions as observed in v_z , the vertical velocity (*top and middle*), and p , the pressure (*bottom*). The gray scale is fixed to the range $[-50\%, +15\%]$, where each map has been normalized by the value of the quiet power in that frequency range. In both simulations, the source distributions are spatially uniform. The qualitative and quantitative differences seen between the first two cases (*top and middle*) could be ascribed to the magnetic field strength, the location of the $\beta = 1$ layer, and the source depth. We use pressure fluctuations as a proxy for observations in intensity. Although more careful studies are required in order to be able to deconstruct these results into participatory elements, it can be said that the computations reproduce many features in the velocity observations (e.g., Moretti et al. 2007).

identification of the nature of these increments and decrements is evidently an important issue.

Another set of power maps is displayed in Figure 6. The top row of panels contains the power maps of the 600 G flux tube, whereas the middle and bottom rows show the results from a simulation with a more realistically endowed sunspot: a 3000 G flux tube (simulation size: $200 \text{ Mm} \times 200 \text{ Mm} \times 35 \text{ Mm}$). The flux tube configuration is very similar to that discussed in Cameron et al. (2007); consequently, we do not show it here. The images in the middle row are strikingly similar in structure to the observations of Moretti et al. (2007), who see power increasing progressively with frequency (Fig. 1 of their paper). We see a large decrease in the rms power as felt by the pressure fluctuations (interpreted crudely as intensity) in the bottom row of panels. There is some qualitative agreement between the simulations and the intensity observations by Moretti et al. (2007); however, the high-resolution *Hinode* measurements of intensity in active regions by Nagashima et al. (2007) are unfortunately not so easily woven into this computational web. Intensity observations, as

Nagashima et al. (2007) note, are far more difficult to interpret than those in velocity because of the former's sensitivity to ionization, pressure, density, etc., and the lack of a one-to-one correspondence with a simple thermodynamic variable.

Acoustic halos around the edges of active regions have been widely observed (e.g., Braun et al. 1992; Brown et al. 1992; Balthasar et al. 1998; Donea et al. 2000). While Balthasar et al. (1998) have reported enhancements in oscillation velocity power within magnetic regions and in low-frequency ($\sim 2 \text{ mHz}$) bandpasses as well, a large number of other observations seem to show halos only in a high-frequency bandpass and in predominantly weakly magnetic areas surrounding the active region (Hindman & Brown 1998). It is interesting to note that some qualitative features also seen in observations are reproduced in the simulations: (1) at the edge of the flux tube (at $\sim 19\text{--}20 \text{ Mm}$ in Fig. 5, $|\mathbf{B}| \sim 7\text{--}12 \text{ G}$), only the highest frequency bandpass shows a faint power enhancement, which is on the order of 2%–3% in v_z and even less in the other components; (2) the increase in the wave power in the umbra of the flux tube in the 4–5 mHz bandpass

(Fig. 5*d*) is similar to enhancements seen in the magnetic cores of active regions (Balthasar et al. 1998); and (3) the enhancements grow with frequency, as can be seen in the simulation of the 3000 G flux tube in Figure 6 and in observations by Moretti et al. (2007). It would be rather ludicrous to make quantitative comparisons between observations and the simulations because of the simplified nature of these calculations: the lack of radiative heat transfer, realistic wave mode damping, a penumbra, convection, unmodeled atmospheric magnetic fields, etc.

The speculation that enhanced seismic emission in the vicinity of active regions may be the causative mechanism of the acoustic halo goes back to the work of Brown et al. (1992). More recently, Donea et al. (2000) have drawn similar conclusions from holography-related analyses of active region observations. However, this theory does not explain the wave power increase in the simulations, because in our calculations, wave source amplitudes are statistically homogeneously distributed in space (in the horizontal directions), with the exception of areas close to the boundaries. Magnetic regions reconfigure the energy of the background medium. Therefore, the presence of sources in the interior of the flux tube essentially complicates matters because the incipient waves may have energies that are unlike those of waves in quiet regions. Moreover, the relative locations of the $\beta = 1$ layer with respect to the acoustic reflection zone, the $\tau = 1$ line, and the sources probably play an extremely important role in determining the wave energy distribution as a function of frequency. All the variables in the simulation are extracted at a constant geometrical height (200 km above the photosphere), which is clearly a simplification incongruent with reality. Whether or not the observation height is a significant contributor is yet to be determined. Further investigations are currently in progress and will be the focus of a future paper.

4. DISCUSSION

We have discussed and validated a numerical method with which to systematically study linear MHD interactions in the context of helioseismology. The importance of including the ambient atmospheric magnetic field in the vicinity of magnetic flux concentrations is underlined here. Through a phenomenological model of the gradient smoothing that the ambient magnetic field presumably effects, we have shown that there can be significant differences in estimates of the oscillation velocity inside active regions. Thus, forward models that attempt to recover the magnetic field distribution on the basis of shifts in travel

times or other helioseismic metrics must in fact address this issue. Computational studies pertaining to oscillation power reduction in active regions are also quite sensitive to these effects.

Results from simulations of waves interacting with flux tubes that have peak photospheric field strengths of 600 and 3000 G are discussed in some detail. Not only is a significant reduction in wave power observed, but a halo that surrounds the flux tube is also seen. Many features in the velocity observations of active regions are reproduced by the simulations. High-frequency wave power halos are also observed to envelop solar active regions; Braun et al. (1992), Brown et al. (1992), and Donea et al. (2000) suggest enhanced seismic emission in the vicinity as being the causative mechanism. However, the simulations contain no such seismic enhancements, indicating that the physics behind the formation of the halo is possibly governed by MHD phenomena. A theory that explains the appearance of these excess oscillations will be discussed in a future publication.

Using the techniques described here, we wish to develop helioseismically consistent forward models of thin flux tubes and sunspots. In the context of thin flux tube models, preliminary investigations have already shown that the peak flux tube magnetic field strengths of about 80 G (Duvall et al. 2006) as observed by the MDI instrument are too small by 2 orders of magnitude to cause the observed wave phase shifts. This is a consequence of the relatively low resolution of the MDI instrument, which is unable to capture flux tubes in the 100–200 km size range (T. Duvall, Jr. 2007, T. Bogdan 2007, and R. Cameron 2007, private communications). Simulations with such small features can be computationally challenging due to resolution restrictions and the associated computational overhead. However, interesting subwavelength physics associated with thin flux tubes, namely, the near-field evanescent modes (the “jacket”; e.g., Bogdan & Cally 1995; Hanasoge et al. 2008) can be studied in greater detail with these simulations. These investigations are exciting, especially when seen in the context of the availability of high-quality observations and the upcoming *Solar Dynamics Observatory* (SDO) mission.

This work was possible with funding from grant HMI NAS5-02139. Thanks to Keiji Hayashi for the instructive discussions related to the CT way of dealing with magnetic fields. Also, thanks to Robert Cameron, Ashley Crouch, Elena Khomenko, Tom Bogdan, and Tom Duvall, Jr. for many useful conversations.

APPENDIX

VALIDATION: TWO-DIMENSIONAL ANALYTICAL SOLUTION

Take a two-dimensional slab of finite thickness (L, L). Let the coordinates be labeled (x, z), and assume the presence of a background magnetic field of the form $\mathbf{B}_0 = B_0(x)\mathbf{e}_z$. The background density is assumed to be unchanged by the magnetic field and is spatially nonvarying; the pressure p_0 is adjusted so that a pressure balance is achieved. We choose a velocity of the form $\mathbf{v} = (v_x\mathbf{e}_x + v_z\mathbf{e}_z) \exp[i(kz - \omega t)]$, where $v_x = v_x(x)$, $v_z = v_z(x)$, k is the wavenumber, ω is the frequency, and t is time. Background quantities are denoted by the subscript “0.” The magnetic field and pressure fluctuations are denoted by \mathbf{B} and p , respectively. Since this solution is used to validate the code, we use the linearized ideal MHD equations, which are equations (1)–(5) without the boundary dissipative Γ or Lorentz force controller ζ terms; we also set the source term $\mathbf{S} = 0$. Starting with the adiabatic energy equation (after incorporating the continuity equation), we have

$$\partial_t p = -c^2 \rho_0 \nabla \cdot \mathbf{v} - v_x \partial_x p_0, \quad (\text{A1})$$

$$c^2 = \frac{\Gamma_1 p_0}{\rho_0}, \quad (\text{A2})$$

$$\partial_x p_0 = -\partial_x \left(\frac{B_0^2}{2} \right), \quad (\text{A3})$$

$$\begin{aligned}
-\frac{1}{\rho_0} \partial_x p &= \frac{1}{i\omega\rho_0} \left[\Gamma_1 \partial_x \left(\frac{B_0^2}{2} \right) (\partial_x v_x + ikv_z) - \Gamma_1 p_0 (\partial_x^2 v_x + ik\partial_x v_z) \right. \\
&\quad \left. + \partial_x v_x \partial_x \left(\frac{B_0^2}{2} \right) + v_x \partial_x^2 \left(\frac{B_0^2}{2} \right) \right] e^{i(kz - \omega t)}, \\
-\frac{1}{\rho_0} \partial_z p &= \frac{k}{\omega\rho_0} \left[-\Gamma_1 p_0 (\partial_x v_x + ikv_z) + v_x \partial_x \left(\frac{B_0^2}{2} \right) \right] e^{i(kz - \omega t)},
\end{aligned}$$

where equation (A3) is the pressure distribution created by balancing the Lorentz force due to the background magnetic field and Γ_1 is the first adiabatic index. Moving on to the x -momentum equation, and applying equation (A4), we find that

$$\begin{aligned}
v_x &= \frac{1}{\rho_0 \omega^2} \left[\Gamma_1 \partial_x \left(\frac{B_0^2}{2} \right) (\partial_x v_x + ikv_z) - \Gamma_1 p_0 (\partial_x^2 v_x + ik\partial_x v_z) + \partial_x v_x \partial_x \left(\frac{B_0^2}{2} \right) \right. \\
&\quad \left. + v_x \partial_x^2 \left(\frac{B_0^2}{2} \right) + k^2 v_x B_0^2 - B_0 \partial_x^2 (v_x B_0) - \partial_x B_0 \partial_x (v_x B_0) \right]. \tag{A6}
\end{aligned}$$

Similarly, upon the application of equation (A5) to the z -momentum equation, it may be verified that

$$ikv_z = \left(\frac{\omega^2}{c^2 k^2} - 1 \right)^{-1} \partial_x v_x, \tag{A7}$$

which leads to the relation

$$\partial_x v_x + ikv_z = \eta(x) \partial_x v_x, \tag{A8}$$

$$\eta(x) = \left(1 - \frac{c^2 k^2}{\omega^2} \right)^{-1}. \tag{A9}$$

Upon further manipulation, a second-order differential equation for the eigenfunction v_x may be obtained:

$$\partial_x^2 v_x + \Theta(x) \partial_x v_x + \Phi(x) v_x = 0, \tag{A10}$$

$$\Theta(x) = \frac{2 - \Gamma_1 \eta^2}{\Gamma_1 p_0 \eta + B_0^2} \partial_x \left(\frac{B_0^2}{2} \right), \tag{A11}$$

$$\Phi(x) = \frac{\rho_0 \omega^2 - k^2 B_0^2}{\Gamma_1 p_0 \eta + B_0^2}. \tag{A12}$$

Equation (A10) was solved using the MATLAB boundary value problem solver `bvp4c`. The boundary conditions were chosen to be $v_x|_{x=0,L} = 0$, with the additional condition of $\partial_x v_x|_{x=0} = 1$ required in order to solve for the eigenvalue ω . Because of the linearity of the problem, there is no loss of generality due to this third condition. We show a sample eigenfunction calculation in Figure 7 for the resonant mode with $\nu = 5.09$ mHz; theory and simulation show good agreement. The background magnetic field was chosen to be $B_0 = \tilde{b}(2x)^{1/2}$, with $\tilde{b} = 71.5$ G Mm $^{-1/2}$, $\Gamma_1 = 1.5$, $p_0 = 1.21 \times 10^5 - B_0^2/2$ dyne cm $^{-2}$, and $\rho_0 = 2.78 \times 10^{-7}$ g cm $^{-3}$, where x is expressed in units of Mm.

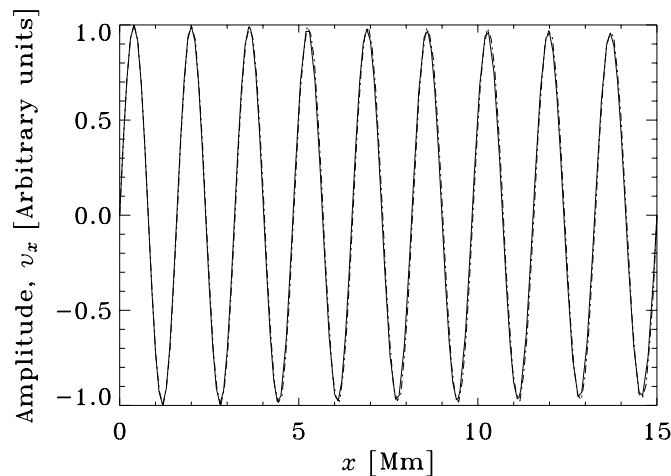


FIG. 7.—Analytically computed (solid line) and numerically simulated (dot-dashed line) normalized eigenfunctions for $\nu = 5.09$ mHz, with $k = 0$. For convenience, the background magnetic field was chosen to be $B_0 = \tilde{b}(2x)^{1/2}$. Although it is not shown here, we have also tested the simulation at nonzero values of k and found good agreement.

REFERENCES

- Abbett, W. P. 2007, *ApJ*, 665, 1469
- Balthasar, H., Martínez Pillet, V., Schleicher, H., & Wöhl, H. 1998, *Sol. Phys.*, 182, 65
- Beliën, A. J. C., Botchev, M. A., Goedbloed, J. P., van der Holst, B., & Keppens, R. 2002, *J. Comput. Phys.*, 182, 91
- Berland, J., Bogey, C., & Bailly, C. 2006, *Comput. Fluids*, 35, 1459
- Bogdan, T. J. 2000, *Sol. Phys.*, 192, 373
- Bogdan, T. J., Brown, T. M., Lites, B. W., & Thomas, J. H. 1993, *ApJ*, 406, 723
- Bogdan, T. J., & Cally, P. S. 1995, *ApJ*, 453, 919
- Bogdan, T. J., Hindman, B. W., Cally, P. S., & Charbonneau, P. 1996, *ApJ*, 465, 406
- Braun, D. C. 1995, *ApJ*, 451, 859
- Braun, D. C., & Birch, A. C. 2006, *ApJ*, 647, L187
- Braun, D. C., Duvall, T. L., Jr., & LaBonte, B. J. 1987, *ApJ*, 319, L27
- Braun, D. C., Lindsey, C., Fan, Y., & Jefferies, S. M. 1992, *ApJ*, 392, 739
- Brown, T. M., Bogdan, T. J., Lites, B. W., & Thomas, J. H. 1992, *ApJ*, 394, L65
- Cally, P. S. 1995, *ApJ*, 451, 372
- . 2000, *Sol. Phys.*, 192, 395
- Cally, P. S., & Bogdan, T. J. 1997, *ApJ*, 486, L67
- Cameron, R., Gizon, L., & Daifallah, K. 2007, *Astron. Nachr.*, 328, 313
- Cattaneo, F. 1999, *ApJ*, 515, L39
- Cheung, M. C. M., Moreno-Insertis, F., & Schüssler, M. 2006, *A&A*, 451, 303
- Christensen-Dalsgaard, J., et al. 1996, *Science*, 272, 1286
- Couvidat, S., Birch, A. C., & Kosovichev, A. G. 2006, *ApJ*, 640, 516
- Crouch, A. D., & Cally, P. S. 2003, *Sol. Phys.*, 214, 201
- Donea, A. C., Lindsey, C., & Braun, D. C. 2000, *Sol. Phys.*, 192, 321
- Duvall, T. L., Jr., Birch, A. C., & Gizon, L. 2006, *ApJ*, 646, 553
- Duvall, T. L., Jr., D'Silva, S., Jefferies, S. M., Harvey, J. W., & Schou, J. 1996, *Nature*, 379, 235
- Duvall, T. L., Jr., Jefferies, S. M., Harvey, J. W., & Pomerantz, M. A. 1993, *Nature*, 362, 430
- Evans, C. R., & Hawley, J. F. 1988, *ApJ*, 332, 659
- Gizon, L., & Birch, A. C. 2002, *ApJ*, 571, 966
- . 2005, *Living Rev. Sol. Phys.*, 2, 6
- Gizon, L., Hanasoge, S. M., & Birch, A. C. 2006, *ApJ*, 643, 549
- Hanasoge, S. M. 2007, Ph.D. thesis, Stanford Univ., <http://soi.stanford.edu/papers/dissertations/hanasoge/>
- Hanasoge, S. M., Birch, A. C., Bogdan, T. J., & Gizon, L. 2008, *ApJ*, 680, 774
- Hanasoge, S. M., Couvidat, S., Rajaguru, S. P., & Birch, A. C. 2007a, preprint (arXiv:0707.1369)
- Hanasoge, S. M., & Duvall, T. L., Jr. 2007, *Astron. Nachr.*, 328, 319
- Hanasoge, S. M., Duvall, T. L., Jr., & Couvidat, S. 2007b, *ApJ*, 664, 1234
- Hanasoge, S. M., et al. 2006, *ApJ*, 648, 1268
- Hindman, B. W., & Brown, T. M. 1998, *ApJ*, 504, 1029
- Hindman, B. W., Jain, R., & Zweibel, E. 1997, *ApJ*, 476, 392
- Khomenko, E., Collados, M., & Felipe, T. 2008, *Sol. Phys.*, in press (arXiv:0710.3335)
- Kosovichev, A. G., & Duvall, T. L., Jr. 1997, in *Proc. SCORE'96: Solar Convection and Oscillations and Their Relationship*, ed. F. P. Pijpers, J. Christensen-Dalsgaard, & C. S. Rosenthal (Dordrecht: Kluwer), 241
- Lele, S. K. 1992, *J. Comput. Phys.*, 103, 16
- Lindsey, C., & Braun, D. C. 2005, *ApJ*, 620, 1107
- Lites, B. W., White, O. R., & Packman, D. 1982, *ApJ*, 253, 386
- Livingston, W., Harvey, J. W., Malanushenko, O. V., & Webster, L. 2006, *Sol. Phys.*, 239, 41
- Moretti, P. F., Jefferies, S. M., Armstrong, J. D., & McIntosh, S. W. 2007, *A&A*, 471, 961
- Nagashima, K., et al. 2007, *PASJ*, 59, S631
- Parchevsky, K., & Kosovichev, A. G. 2007a, *ApJ*, 666, 547
- . 2007b, *ApJ*, 666, L53
- Pizzo, V. J. 1990, *ApJ*, 365, 764
- Pneuman, G. W., Solanki, S. K., & Stenflo, J. O. 1986, *A&A*, 154, 231
- Rosenthal, C. S., & Julien, K. A. 2000, *ApJ*, 532, 1230
- Scherrer, P. H., et al. 1995, *Sol. Phys.*, 162, 129
- Schlüter, A., & Temesváry, S. 1958, in *IAU Symp. 6, Electromagnetic Phenomena in Cosmical Physics*, ed. B. Lehnert (Cambridge: Cambridge Univ. Press), 263
- Schunker, H., Braun, D. C., Cally, P. S., & Lindsey, C. 2005, *ApJ*, 621, L149
- Schüssler, M., & Rempel, M. 2005, *A&A*, 441, 337
- Shelyag, S., Erdélyi, R., & Thompson, M. J. 2007, *A&A*, 469, 1101
- Tóth, G. 2000, *J. Comput. Phys.*, 161, 605
- Zhao, J., & Kosovichev, A. G. 2006, *ApJ*, 643, 1317